nature communications

Article

https://doi.org/10.1038/s41467-025-57086-0

A dynamic isotope effect in the nucleophilic substitution reaction between F^- and CD_3I

Received: 28 November 2023

Accepted: 11 February 2025

Published online: 08 March 2025

Check for updates

Atilay Ayasli[1], Arnab Khan[1,6], Thomas Gstir[1], Tim Michaelsen[1], Dóra Papp[2], Yan Wang[3,4], Hongwei Song[4], Minghui Yang[4,5], Gábor Czakó[2] & Roland Wester[1]

The influence of quantum mechanics on the dynamics of chemical reactions is unknown for many processes in chemistry. Chemical reaction dynamics are often well described by quasiclassical motion of the atoms on quantum mechanical Born-Oppenheimer potential energy surfaces. Here we present a dynamic isotope effect in a nucleophilic substitution reaction experiment that can only be explained by quasiclassical trajectory simulations for reactants containing deuterium atoms, but not when hydrogen atoms are involved. The calculated energy- and angle-differential cross sections are compared to experimental crossed-beam velocity map imaging data, which show significantly more forward scattering for hydrogenated compared to deuterated reactants. Quantum scattering calculations in reduced dimensions explain this by an increased reaction probability for large total angular momentum, a feature that is not captured in the quasiclassical approach.

Understanding a chemical reaction demands detailed insight into how it evolves from reactants to products at an atomistic level. On a complex potential energy landscape, a reaction outcome depends on the pathways that connect reactants to products. Acid-base reactions, addition, elimination, and substitution are four well-known reaction types that cover most of the discussions in organic chemistry textbooks. Bimolecular nucleophilic substitution (S_N2) is such a reaction that, over the years, has served as a prototype to unravel the atomistic dynamics, energetics, and reactivity of chemical reactions related to synthesis in organic and bio-chemistry[1–6]. Reactions of halide anions with methyl halides ($X^- + CH_3Y \rightarrow CH_3X + Y^-$) represent the simplest model system for S_N2 reactions. Many different direct reaction mechanisms such as stripping, rebound, and front-side attack, as well as indirect mechanisms as the roundabout, complex formation, barrier recrossing, and double inversion could be identified[7–12].

Up to now the vast majority of chemical reaction dynamics are described using quasiclassical trajectory (QCT) simulations on multidimensional Born-Oppenheimer potential energy surfaces (PESs). Good agreement has been found for a variety of chemical reactions[13–18]. Quantum mechanical effects on the dynamics of the atomic nuclei on the Born-Oppenheimer PES have been a long-standing research topic[19]. They are, however, challenging to reveal and have so far only been identified in reaction processes with three or four light atoms[20–24]. Larger systems have only rarely been treated with full-dimensional quantum scattering calculations[25]. It is therefore difficult to assess in how far quantum effects, such as tunneling of light hydrogen atoms or quantum resonances due to discrete vibrational eigenstates, are effective in polyatomic reactions.

Isotopic substitution is an important approach for testing the validity of the Born-Oppenheimer surface in molecular spectroscopy. In reaction dynamics it allows one to search for effects not captured by

[1]Institut für Ionenphysik und Angewandte Physik, Universität Innsbruck, Innsbruck, Austria. [2]MTA-SZTE Lendület "Momentum" Computational Reaction Dynamics Research Group, Interdisciplinary Excellence Centre and Department of Physical Chemistry and Materials Science, Institute of Chemistry, University of Szeged, Szeged, Hungary. [3]School of Chemical and Environmental Engineering, Hubei Minzu University, Enshi, China. [4]Key Laboratory of Magnetic Resonance in Biological Systems, State Key Laboratory of Magnetic Resonance and Atomic and Molecular Physics, National Center for Magnetic Resonance in Wuhan, Wuhan Institute of Physics and Mathematics, Innovation Academy for Precision Measurement Science and Technology, Chinese Academy of Sciences, Wuhan, China. [5]Wuhan National Laboratory for Optoelectronics, Huazhong University of Science and Technology, Wuhan, China. [6]Present address: Department of Physics, Indian Institute of Science Education and Research (IISER), Bhopal, India. e-mail: roland.wester@uibk.ac.at

QCT simulations. The effect of isotopic exchange is frequently discussed for reaction rates and is known as the kinetic isotope effect (KIE), defined as the ratio of the reaction rate coefficients for hydrogen versus deuterium-containing reactants. The KIE may occur through lowering of the zero-point energy (ZPE), which causes a reaction after deuterium replacement to require a different energy to cross a potential barrier and thereby renders it sensitive to the transition-state structure as well as the temperature[26]. In S_N2 reactions, inverse KIEs (smaller than one) have been measured for a range of systems[27–29]. High-level quantum dynamics calculations have found both normal and inverse isotope effects for the $H + CH_4$ reaction, which are explained by inefficient energy transfer between translational and vibrational motion[30] that may bear similarities with negative-ion S_N2 reactions.

Reaction dynamics under isotopic exchange have been studied for the neutral $OH + CH_4$ system and its isotopic variants using the crossed molecular beam method[31]. A notable change in the stretching excitation for the deuterated system was observed, while the excitation in bending and other modes is not significant. This result suggested that isotopic exchange has 'quite subtle' effects on the product angular distributions and the secondary-KIE only affects the vibrational distribution of the water products[31]. These experimental results were theoretically supported by QCT calculations using an analytical full-dimensional PES[32], which showed that QCT simulations had a better match with the experiment for the deuterated case. The conclusion was that due to the more 'local' character of the HOD stretching and less influence from tunneling, the reaction with the deuterated counterpart matches better with the QCT calculation than for H_2O.

Quantum effects in reaction dynamics have also been explored by investigating the vibrational specificity of chemical reactions after exciting a single quantum of a selected vibrational mode[33,34]. The $F^- + CH_3I$ collision system[9,35–37] showed that the symmetric CH stretching vibration of the neutral acts as a spectator for the S_N2 reactivity at a relative collision energy of 0.7 eV, while an enhancement has been observed with the increase in collision energy[38,39]. This 'spectator' mode character implies that this mode is weakly coupled to the reaction coordinate and does not influence the reactivity, while an overall enhancement has been observed for the proton transfer channel with CH stretching excitation[40]. Unlike most $X^- + CH_3Y$ S_N2 reactions, the pre-reaction complex is not co-linear in this case, but the F^- first attaches to one of the three H-atoms[36].

In this work we study the reaction dynamics of the nucleophilic substitution and deuteron transfer channels in the following reactions:

$$F^- + CD_3I \rightarrow CD_3F + I^- \quad \Delta H = -1.96\,\text{eV} \tag{1}$$

$$F^- + CD_3I \rightarrow FD + CD_2I^- \quad \Delta H = 0.72\,\text{eV}, \tag{2}$$

where the enthalpies are taken from ref. 37, corrected for the ZPE of the deuterated species. The results are compared to recent data for the corresponding hydrogenated reactions[39,40], as well as to QCT and quantum dynamics calculations. In this multifaceted comparison, we find quantitative agreement between experiment and QCT simulations for the deuterated reaction but distinct differences in the hydrogenated reaction. This allowed us to identify that non-classical effects modify the orbital angular momentum-dependent reaction dynamics for the hydrogenated reactant.

Results

The experimental energy- and angle-dependent differential scattering cross sections have been obtained for the anionic reaction products I^- and CD_2I^- of the reactions (1) and (2) using a crossed-beam velocity map imaging spectrometer (see Methods section). We also present scattering data for the products of the reaction of fluorine anions with hydrogenated methyl iodide CH_3I from previous publications[39,40] for comparison with the deuterated measurements. The reactive scattering experiments have been conducted under single-collision conditions for collision energies E_{rel} ranging from 0.7 to 2.3 eV with an average energy width of 180 meV (FWHM). The setup and the experimental procedures are described in the methods section. Full-dimensional QCT simulations and reduced-dimensional quantum scattering calculations, described in the methods section, are also presented. Throughout this article, reactive collisions of F^- with CD_3I will be referred to as the deuterated reaction, and with CH_3I as the hydrogenated reaction.

S_N2 reaction dynamics

Experimental results for the S_N2 channel, reaction (1), are presented in Figs. 1 and 2. Figure 1 shows the angle- and velocity differential cross sections for the product I^-. The first row of Fig. 1(a1–a4) presents three-dimensional velocity distributions of I^- products from CD_3I as a target molecule, projected onto the two-dimensional scattering plane. The second row (b1–b4) are iodide anions resulting from the isotopologue CH_3I[39]. The outermost circles superimposed on each figure mark the kinematic cutoff for each dataset, representing the maximum velocity achievable given the conservation of energy and momentum in the reaction. The figures are represented in the center-of-mass frame of the collision. Reactant ions move from left to right in our chosen reference frame and the neutral reactant from right to left. This defines the forward direction for detected product ions on the left-hand side of each image.

We extracted the angular and internal energy distributions from the cross section data, as shown in Fig. 2. The first row (a1–a4) are velocity-integrated angular distributions of the product I^- resulting from scattering of F^- with CD_3I (red) and CH_3I (blue). The forward and backward directions are matched to the cross-sectional data, which is why the data is plotted as $-\cos(\theta)$. The panels in the third row (c1–c4) in Fig. 2 represent experimentally obtained internal energy distributions of CD_3F (red) and CH_3F (blue) product molecules.

Starting at the lowest collision energy of 0.7 eV, the deuterated system shows three distinct reaction mechanisms visible in the differential cross section and, more quantitatively, in the velocity-integrated angular distributions. These are: Direct backscattered products at higher velocities close to the kinematic cutoff, direct forward scattered products at intermediate and isotropically scattered products at low velocities. The umbrella-like signature in the backward hemisphere can be assigned to the direct rebound mechanism[9,41], which corresponds to the classic textbook description of an S_N2 reaction, where a Walden inversion takes place[42]. Back-scattered events like this require small impact parameter collisions[5]. At intermediate velocities, a direct forward scattering signature is visible on the left side of the images. These forward scattered events are characteristic of a stripping mechanism. Stripping mechanisms are large impact parameter events where the product is only slightly deflected[8]. Finally, at the lowest product velocities, isotropically scattered ions are observed. These are representative of an indirect mechanism, where the reactant ion and neutral form a complex that has longer lifetimes than one average rotation and dissociates statistically. The complex-forming mechanism coincides with slower products and therefore high internal excitation of the neutral CD_3F. The internal energy distribution at 0.7 eV (Fig. 2, panel c1) shows that highly excited products emerging from indirect mechanisms are the preferred outcome at this collision energy.

We have quantified the contribution of each reaction mechanism for both deuterated and hydrogenated reactions at each collision energy (see Fig. 1 and supplementary information). The results with their estimated accuracies are presented in Table 1. At the lowest collision energy, isotropic scattering has the largest contribution with 51(9)% for the deuterated reaction. Forward scattered events have the lowest contribution with 17(4)%. The third mechanism, direct rebound,

https://doi.org/10.1038/s41467-025-57086-0

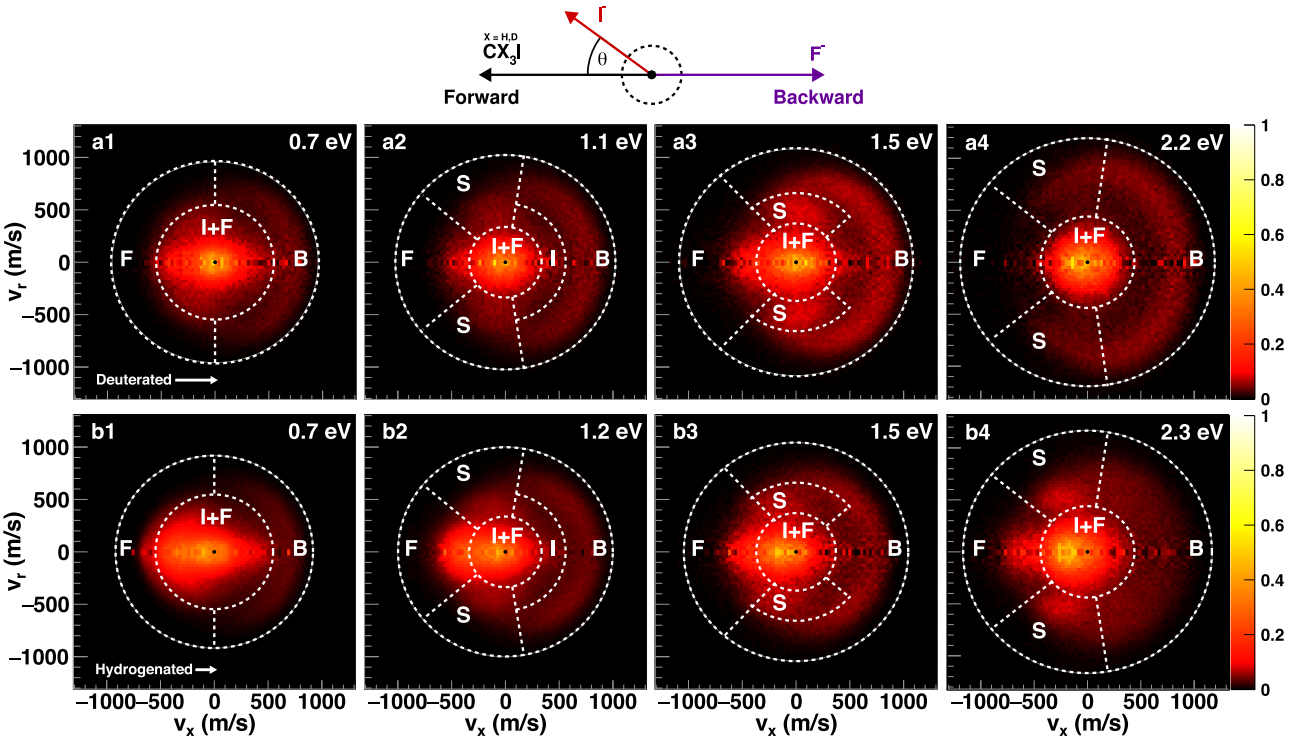

Fig. 1 | Measured differential scattering cross sections for the S_N2 reaction. Row (**a**) depicts I^- products resulting from $F^- + CD_3I$, while row (**b**) shows products from the hydrogenated reaction $F^- + CH_3I$ [the data for panels b1, b2, and b4 are replotted from ref. 39]. The I^- velocity distributions are depicted in the center-of-mass frame at four different relative collision energies ranging from 0.7 to 2.3 eV. The outermost rings mark the kinematic cutoff, representing the maximum velocity an I^- can achieve at the given initial F^- and CH_3I/CD_3I velocities. The dashed lines mark the segmentation of the images to quantify the contributions of different mechanisms due to (F)orward, (S)ideways, (I)ndirect, and (B)ack scattering (see supplementary information for details). The Newton diagram at the top depicts the relative orientation for the velocity vectors of both reactants and I^-. Source data are provided as a Source Data file.

is found in 33(4)% of the events. At the higher collision energy of 1.2 eV, we are able to differentiate an additional reaction mechanism in the deuterated reaction. Here, products are observed that are deflected towards large sideways angles of near 90°, referred to as sideways scattering. Upon increasing the relative collision energy, the contribution of isotropic scattering, the dominant mechanism at low energies, decreases, while back-scattered direct rebound contribution increases. Direct sideways scattering remains roughly constant over the entire deuterated dataset. Forward scattered products nearly vanish at the highest collision energy.

To gain additional insight, we performed QCT simulations for the deuterated system and its isotopologue using a multidimensional potential energy surface[37] (see Methods section). Computed angular and internal energy distributions at each collision energy are presented in the second row (b1–b4) and fourth row (d1–d4) of Fig. 2, respectively. Comparing experimental and theoretical results shows an excellent agreement in angular and internal energy distributions for the deuterated reaction, with all features being reproduced with high fidelity.

When turning to the hydrogenated case, the same reaction mechanisms as discussed above can be identified (see Table 1). A similar shift from indirect towards more direct dynamics is seen with increasing collision energy, with direct rebound and sideways scattering being the prevalent reaction mechanisms at higher energies. The hydrogenated scattering cross section shows significantly more direct forward scattering dynamics with a correspondingly reduced number of back-scattered events. Specifically, about 10% of counts in the hydrogenated case lead to additional forward scattering, while back-scattering sees on average about 10% less counts (see Table 1). This is also directly visible in the experimental angular distributions in Fig. 2, (a1–a4). In a direct comparison between the hydrogenated reaction (blue line) and the deuterated reaction (red line), the former clearly shows strong enhancement of forward scattering dynamics. The enhancement of forward scattering is also visible in the internal energy distribution for CH_3F (blue) and CD_3F (red). The hydrogenated system forms neutral products with higher internal excitation than its deuterated counterpart. This is illustrated by a visual comparison in panel c4 of Fig. 2. The deuterated reaction shows a clear bimodal structure through the shift towards more direct dynamics, where the first lower peak corresponds to products formed by the direct rebound mechanism and the second peak shows high internal product excitation through indirect mechanisms. The minimum in between is the internal energy range where we would expect CD_3F products resulting from forward scattering. This is filled in the hydrogenated reaction and only a barely significant dip at large internal excitation is remaining.

The QCT calculations for the hydrogenated reaction also show an overall agreement with the measurement. But there is one important difference between experiment and theory: The strongly enhanced forward scattering mechanism is not reproduced in the simulations for CH_3I. This is further discussed below.

Deuteron transfer reaction dynamics

We also present differential velocity- and angle-dependent cross sections for both deuteron and proton transfer reactions (reaction (2)), taken together with the S_N2 data at the same relative collision energies, see Fig. 3. Panels (a1–a3) depict CD_2I^- products stemming from the deuteron transfer reaction $F^- + CD_3I \rightarrow DF + CD_2I^-$, panels (b1–b3) show CH_2I^- product ions of the isotopologue. The experimental and simulated angular and internal energy distributions are shown in Fig. 4.

Both CD_2I^- and CH_2I^- can be barely observed at a relative collision energy of 0.7 eV, which corresponds to the enthalpy of both reactions.

https://doi.org/10.1038/s41467-025-57086-0

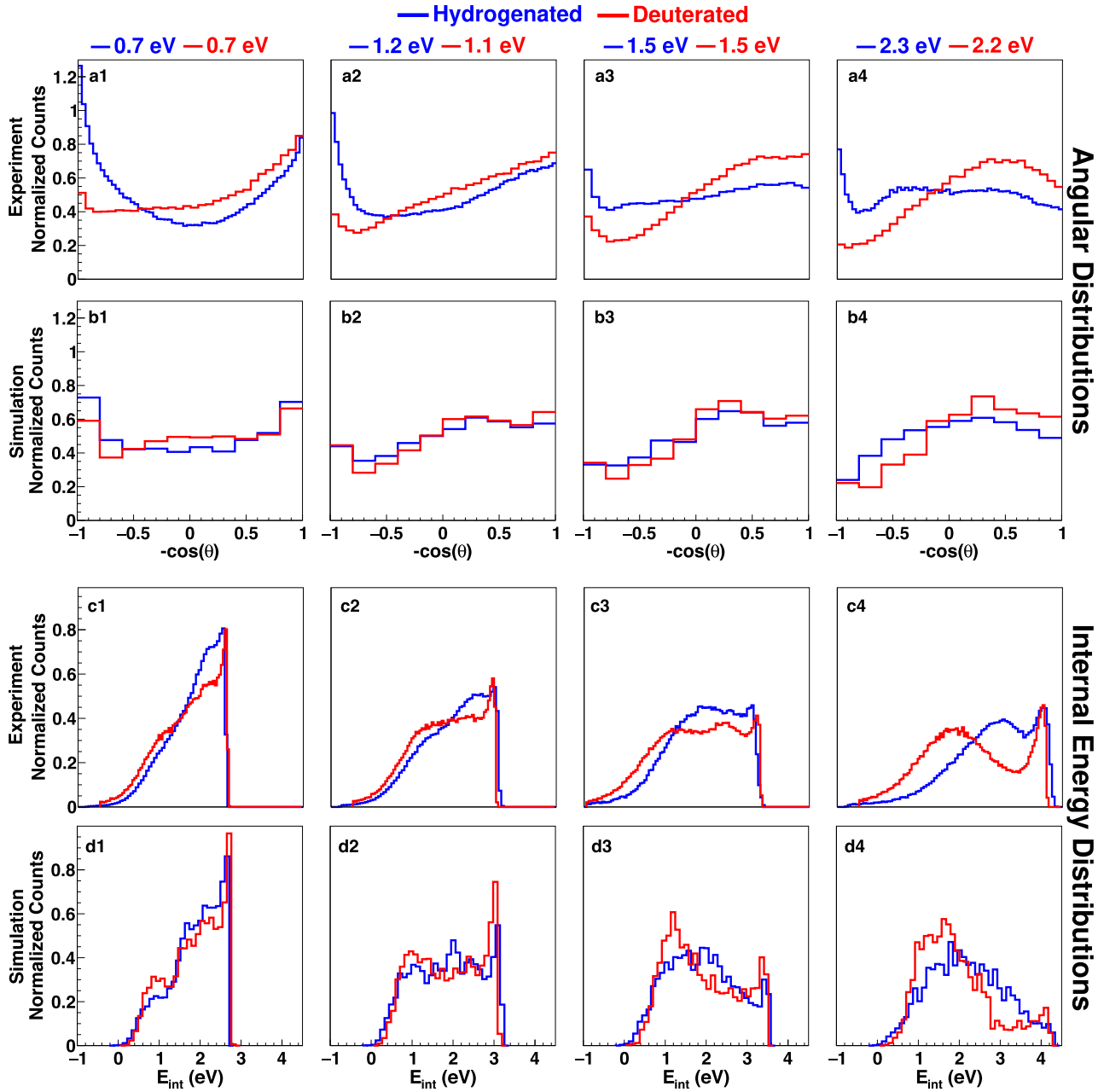

Fig. 2 | Angular and internal energy distributions for the S_N2 reactions of $F^- + CH_3I$ (blue) and $F^- + CD_3I$ (red) at different relative collision energies ranging from 0.7 to 2.3 eV. Row **a**: Velocity integrated angular distributions extracted from differential cross sections. Row **b**: Calculated quasi-classical trajectory (QCT) angular distribution of hydrogenated and deuterated S_N2 type reactions. Row **c**: Derived internal energy distributions of the CH_3F (blue) and CD_3F (red) product molecules. Row **d**: Calculated (QCT) product internal energy distributions. Source data are provided as a Source Data file.

As a consequence, the statistics are too low for meaningful analysis at this energy. The appearance of products close to threshold is due to the absence of a transition state barrier above the product energy[43]. While S_N2 is the predominant reaction channel throughout all measured collision energies, the proton and deuteron transfer channels increase in relative strength at higher collision energies. The trend of both reactions is a shift from isotropically scattered events at low collision energy to purely forward scattered large-impact parameter events. This is in line with previous results on proton transfer[40,44]. Slight differences also appear in the data; there is slightly more forward scattering for proton transfer and, in contrast, more backward scattering for deuteron transfer.

Figure 4 also presents QCT simulations for comparison. Both angular and internal energy distributions show a very good agreement with the measured data. Notably, also the differences in the angular distribution for proton and deuteron transfer are correctly captured by the simulations.

Calculated reaction probabilities

Further information on the S_N2 channel of the hydrogenated and deuterated reactions is obtained from reduced dimensional quantum scattering calculations. For this, the reaction is studied using the initial state-selected time-dependent quantum wave packet method on the same PES[37] used for the QCT simulations (see Methods section and supplementary information for details). The CH_3I moiety is assumed to maintain the C_{3v} symmetry and six important degrees of freedom relevant to the S_N2 reaction are treated explicitly. In addition to the scattering coordinate, these are the C-I stretching, CH_3 symmetric

stretching and umbrella bending modes, and the rotational degrees of freedom of CH_3I.

The reaction probabilities as a function of total angular momentum, obtained from the quantum dynamics calculations, are plotted in Fig. 5, panels a–d, for the ground rovibrational states of CH_3I and CD_3I at the four studied collision energies. In the same figure also the opacity functions obtained from the QCT simulations for CH_3I and CD_3I are plotted. For both hydrogenated and deuterated reactions, the quantum dynamics results show very different reaction probabilities than the QCT results, in particular visibly larger probabilities for higher angular momenta. Between hydrogenated and deuterated reaction the quantum dynamics result differs by around a factor of two, while the QCT results differ by around 20%. Furthermore, for collision energies of 1.2 eV and above the quantum reaction probability vanishes for slightly smaller total angular momenta for the deuterated compared to the hydrogenated reaction. The integral cross sections (see Fig. S2) obtained by the quantum dynamics calculations are a factor of two larger than the QCT results for both hydrogenated and deuterated reactants, which is further discussed below. The experimental results at 0.7 and 1.0 eV[35] (also shown in Fig. S2) lie in between the calculated values.

Table 1 | Different reaction mechanisms assigned to both deuterated and hydrogenated differential cross sections in the energy range of 0.7–2.3 eV

		Hydrogenated	Deuterated	Difference
Forward scattering	0.7 eV	29(5)%	17(4)%	13(1)%
	1.2 eV	15(3)%	6(1)%	9(3)%
	1.5 eV	16(2)%	7(1)%	9(3)%
	2.3 eV	13(2)%	3(1)%	10(2)%
Sideways scattering	1.2 eV	29(2)%	33(2)%	−4(1)%
	1.5 eV	37(3)%	32(3)%	4(1)%
	2.3 eV	36(2)%	33(1)%	3(1)%
Direct rebound	0.7 eV	24(5)%	33(4)%	−9(1)%
	1.2 eV	32(3)%	38(3)%	−6(1)%
	1.5 eV	35(5)%	45(4)%	−10(1)%
	2.3 eV	34(2)%	48(1)%	−14(1)%
Indirect mechanism	0.7 eV	47(6)%	51(9)%	−4(2)%
	1.2 eV	24(3)%	23(5)%	1(2)%
	1.5 eV	12(3)%	15(3)%	−3(1)%
	2.3 eV	17(4)%	15(3)%	2(1)%

The values have been rounded to the nearest integer value.

Discussion

We observe a shift from direct backward to forward scattering when the deuterium atoms in the $F^- + CD_3I$ reaction are isotopically substituted by hydrogen atoms, which we refer to as a dynamic isotope effect. The difference is found at all collision energies and the relative change is estimated to make up around 10% of observed events. QCT calculations can reproduce all features observed in the deuterated reaction with high fidelity, but do not fully reproduce the hydrogenated reaction. This deviation only occurs for the S_N2 reactions. The measured proton and deuteron transfer channels also show differences, but these are in very good agreement with the QCT calculations. Here, the C-H or C-D bond is directly affected, which suggests a more subtle difference for the S_N2 channel. Supposed that the discrepancy between experiment and simulation is due to the quasiclassical nature of the calculated trajectories, we can expect a quantum mechanical effect to be the cause for the difference. The dipole moments of CH_3I and CD_3I are almost the same (1.6406(4) D and 1.6507(4) D, respectively[45]). Therefore the long-range interactions with F^- are very

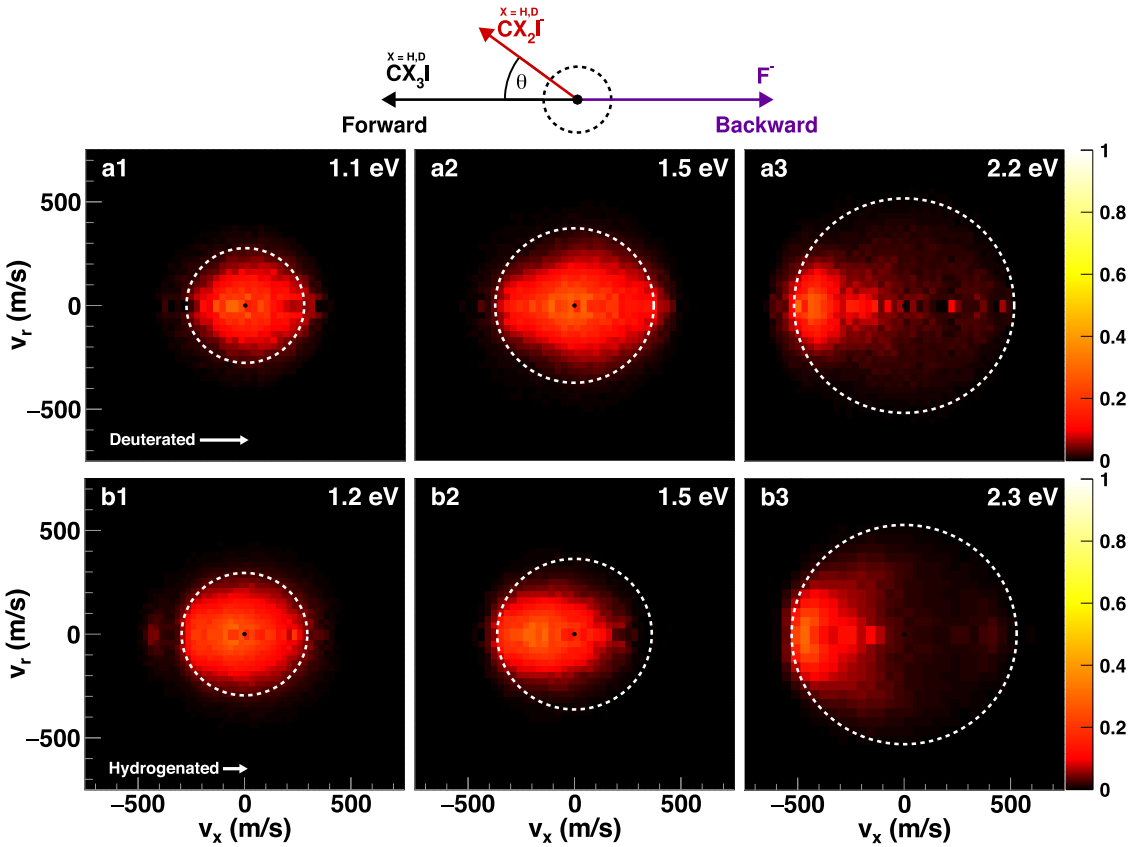

Fig. 3 | Measured differential scattering cross sections for the proton ($F^- + CH_3I$) and deuteron transfer ($F^- + CD_3I$) reactions. Row (**a**) depicts CD_2I^- products, while row (**b**) shows CH_2I^- [the data for panels b1 and b3 are replotted from ref. 40]. The data are presented in the same manner as Fig. 1. Source data are provided as a Source Data file.

https://doi.org/10.1038/s41467-025-57086-0

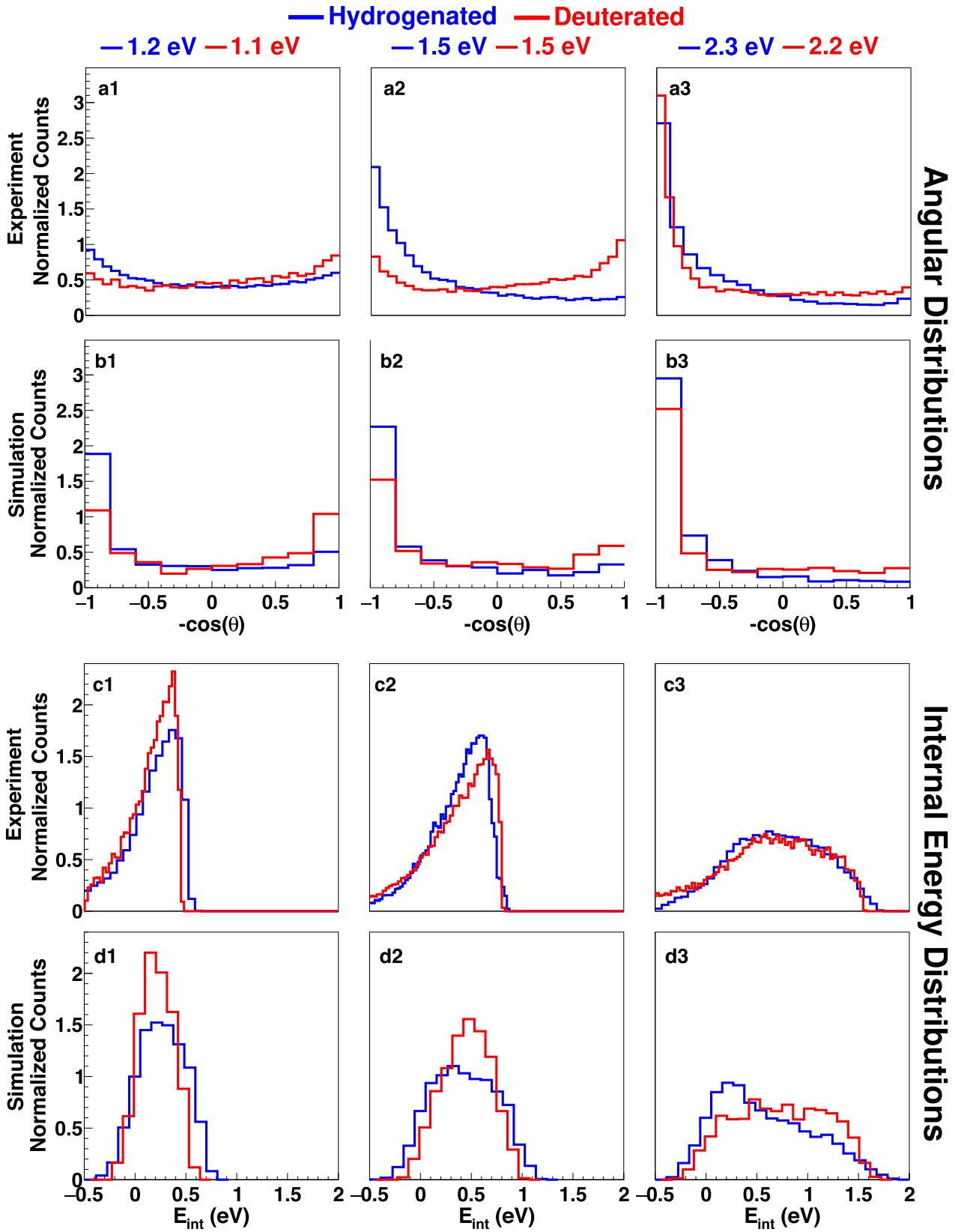

Fig. 4 | Angular and internal energy distributions for the proton transfer (blue) and deuteron transfer reactions (red) at different relative collision energies. The data are presented in the same manner as Fig. 2. Row **a**: Velocity integrated angular distributions extracted from differential cross sections. Row **b**: Quasi-classical trajectory (QCT) calculations simulating the angular distribution of both proton and deuteron transfer. Row **c**: Derived internal energy distributions Row **d**: Simulated (QCT) product internal energy distributions. Source data are provided as a Source Data file.

https://doi.org/10.1038/s41467-025-57086-0

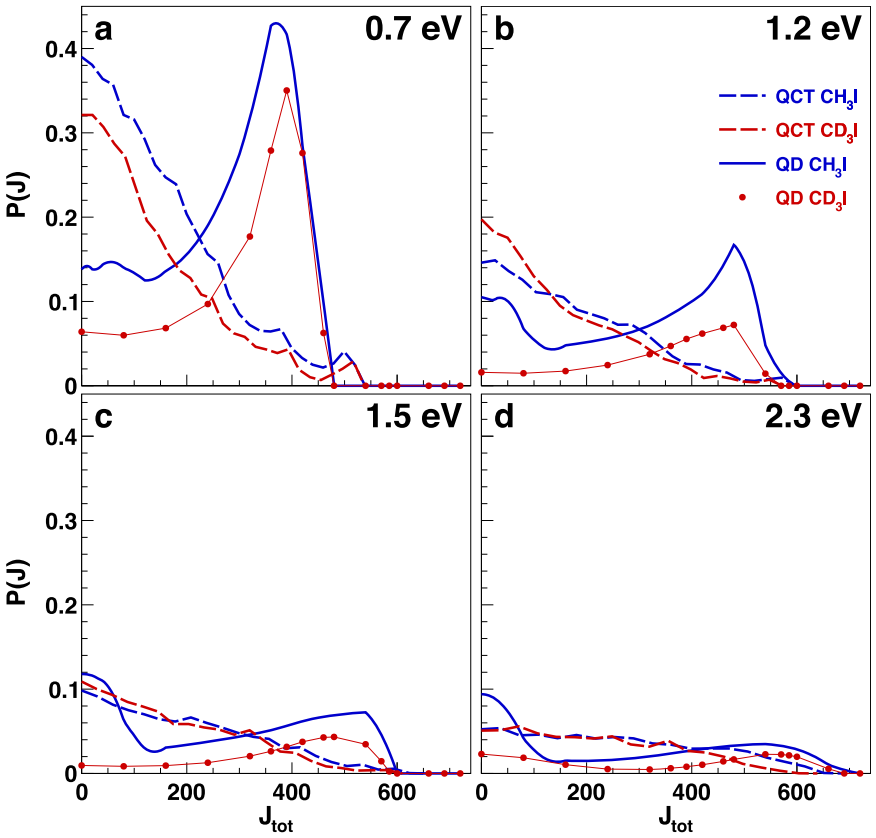

Fig. 5 | Calculated opacity functions. Opacity functions for the hydrogenated (blue) and deuterated (red) S_N2 reactions ($F^- + CH_3I$ / CD_3I) at four different collision energies (panels **a**: 0.7 eV, **b**: 1.2 eV, **c**: 1.5 eV, and **d**: 2.3 eV) using a quantum scattering approach (solid lines) and quasiclassical trajectories (dashed lines) as a function of the total angular momentum J_{tot}. Source data are provided as a Source Data file.

similar and cannot introduce an isotope effect. This statement is true for high angular momenta as well, because the reduced masses of the $F^- + CH_3I/CD_3I$ systems are also almost the same. Note that the measured total reaction rate coefficient for the title reaction at 300 K is close to the Langevin limit for both hydrogenated and deuterated reactions[27], showing the absence of a KIE at room temperature. In contrast, the rate coefficient decreases far below the capture limit at collision energies above a few hundred meV[35]. This bodes well with the present findings of a much higher reaction probability for the hydrogenated reaction than for the deuterated reaction.

The quantum dynamics calculations show that the reaction probability is much larger at large orbital angular momentum than extracted from the QCT simulations, leading to an overall larger integral cross section by a factor of two compared to the QCT integral cross section. One way this can be explained is via the effective potential energy barrier, which increases as the impact parameter or, correspondingly, the total angular momentum increases. Although the S_N2 reaction is intrinsically barrierless, it is mediated by the effective potential, defined as the sum of the potential energy and the centrifugal potential along the minimum energy path. The effect of the centrifugal barrier is expected to be maximal at the Walden-inversion barrier, where the intermolecular distance of the reactants is minimal. When the total angular momentum increases to a certain value (around 300$\hbar$) in the reaction, the effective potential energy barrier for the S_N2 reaction becomes positive. The barrier height is essentially the same for the hydrogenated and the deuterated reactions due to the only slight difference in the reduced masses of the two systems. However, near and above the reaction threshold quantum tunneling may become relevant, which could explain the non-zero quantum reaction probability at the largest angular momenta relevant for the hydrogenated S_N2 reaction, most visible at 1.2 eV collision energy, where the deuterated reaction probability already vanishes (see Fig. 5b). These large impact parameters are expected to preferentially lead to forward scattering, in qualitative agreement with the experimental observation for the hydrogenated reaction. Note, however, that the quantum dynamics calculations do not include the proton/deuteron transfer channel, which is smaller in probability than the substitution channel, but still of significant magnitude. It is therefore likely that some reactants that would undergo proton/deuteron transfer are drawn towards the S_N2 product channel, enhancing unphysically the reactivity of the S_N2 reaction. For the proton or deuteron transfer channel, due to the deep pre-reaction well and its endothermicity, it is unlikely that quantum tunneling plays a significant role.

The much higher density of states in the deuterated reaction could also facilitate more direct dynamics as more efficient vibrational coupling could shorten the lifetimes of intermediate complexes. For example, it has been seen that for the $Cl^- + CH_3Cl$ system, the substitution of H by D decreases the barrier recrossing rate substantially due to the faster rate for intramolecular vibrational energy redistribution (IVR)[46]. If the vibrational coupling is reduced in the hydrogenated reaction that may not be fully captured in the QCT simulations, which tend to overestimate the rates for IVR in reaction complexes[47,48].

In reactive scattering experiments of F^- with vibrationally excited CH_3I[39,40], we have observed changes in the dynamics and reactivity after exciting the symmetric CH-stretching vibration in CH_3I, which could also not be fully reproduced by QCT simulations[49], using the same PES as in the present QCT calculations. This provides further evidence that the coupling of the vibrational modes in the

hydrogenated reaction complex may be sensitive to the quantum mechanical density of states. In the future, full-dimensional quantum dynamics calculations are expected to resolve these differences. These are presently becoming possible for six-atomic systems, at least for zero total angular momentum and only two heavy atoms[25]. Alternatively, approximate quantum methods such as ring polymer molecular dynamics simulations[50] may be useful to shed light on the identified quantum effects in nucleophilic substitution reactions.

In summary, we have obtained experimental differential cross sections for the reaction of $F^- + CD_3I$ for both the S_N2 and deuteron transfer pathways. These are compared to experimental data for the same pathways in the $F^- + CH_3I$ reaction, full-dimensional QCT calculations for both pathways, and reduced-dimensional quantum scattering calculations for the S_N2 channel using the same PES. The QCT calculations reproduce the experimental results for the deuterated reaction very well, but in the hydrogenated case the comparison highlights a clear difference in the differential cross sections. Backward scattered, direct rebound is shifted to forward scattering when moving from the deuterated to the hydrogenated nucleophilic substitution reaction. Whereas most features of the deuteron and proton transfer dynamics are captured by the QCT calculations, the enhanced forward scattering for the S_N2 channel is not reproduced.

In the absence of an agreement with quasiclassical dynamics, this dynamic isotope effect is assigned to a quantum mechanical effect, which is qualitatively supported by quantum dynamics calculations in reduced dimensions. Compared to the deuterated reaction, these calculations show a slightly enhanced reaction probability of the hydrogenated reaction at large angular momenta, where the forward-scattering mechanism is favored. The preference of large angular momenta in the hydrogenated S_N2 reaction over the deuterated one may be attributed to tunneling through a positive effective barrier in the hydrogenated case, formed from the sum of the Walden-inversion barrier, involving the umbrella motion of the hydrogen atoms in the CH_3 unit, and the centrifugal potential.

Quantum dynamical effects, as found in the present case, may be more prevalent than currently expected given the success of QCT simulations to accurately describe gas phase chemical dynamics. With more and more high- or even full-dimensional quantum scattering calculations for reactions of polyatomic molecules, it will be an important task to search for such effects. This is particularly important for reactions where hydrogen atoms are involved, even if their involvement is only indirect as in the case of nucleophilic substitution.

Methods

Experiment

We employ velocity map imaging in a crossed-beam setup to record angle- and velocity dependent differential cross sections of reactive ion-molecule collisions[9,51–53].

To create the reactant ions, a 10% mixture of NF_3 seeded in argon is used as a precursor gas. A home-built cantilever piezo valve is used to produce F^- ions via dissociative electron attachment in a pulsed plasma discharge. The average pulse length is varied between 30 and 80 μs at switched DC-voltages of around 700 V, depending on the stability of the ion signal. The ions are extracted perpendicularly to the initial direction in a Wiley-Mclaren-type electrode configuration for mass selection. An octupole radiofrequency ion trap is subsequently used to trap the ions along the experimental axis for tens of milliseconds. Helium buffer gas thermalizes the trapped ion ensemble to room temperature inside the trap, which reduces the energy spread of the ion beam. The ions are then extracted and decelerated to desired kinetic energies and crossed with a neutral beam of CH_3I or CD_3I in the interaction region of the spectrometer at a crossing angle in the laboratory frame of 60°. The laboratory kinetic energies, recorded with two-dimensional velocity map imaging, were tuned to between 1.1 and 3.0 eV, with about 160 meV FWHM. Combined with the neutral beam velocity, this led to relative collision energies between 0.7 and 2.3 eV with an average accuracy of 180 meV (FWHM).

The neutral beam is produced via supersonic expansion in a differentially pumped neutral beam chamber. For the hydrogenated (deuterated) reaction experiment a mixture of 5% methyliodine (methyliodine-D_3) seeded in helium is used to create the neutral beam. To prevent clustering in the neutral beam and to avoid condensation inside the nozzle, a backing pressure of 0.7 bar on a heated nozzle at 60 °C was used for the neutral beam. The resulting neutral beam velocity, typically (1100 ± 100) m/s, is measured frequently during data acqusition using electron impact ionization and two-dimensional velocity map imaging, in order to identify possible velocity drifts. The setup is operated at a repetition rate of 20 Hz. Reaction products are mapped onto a time- and position sensitive detector. For each reactive event the recorded position and time information are transformed into a velocity vector and product mass in the center-of-mass frame.

From this velocity vector histograms of the scattering angle, the internal energy in the molecular product, and images of the differential cross section in the scattering plane are produced. The cross section images are plotted as a function of the velocity component parallel (v_x) and perpendicular (v_r) to the reactant's relative velocity axis (see the Newton diagram in Fig. 1). Each entry is weighted with $1/v_r$ to create an image that corresponds to a sliced image through the three-dimensional scattering distribution, such that isotropic scattering is representend by a homogeneous intensity.

Quasiclassical trajectory calculations

QCT computations were performed for the $F^- + CH_3I$ and $F^- + CD_3I$ reactions at 0.71, 1.20, 1.57, and 2.33 eV and 0.76, 1.10, 1.50, and 2.24 eV collision energies, respectively, using our own dynamics code and a recently-developed full-dimensional high-level ab initio analytical PES[37]. The initial distance of the reactants is $\sqrt{x^2 + b^2}$, where $x = 30.0$ bohr. The impact parameter b varies between 0.0 and b_{max}, where the reaction probabilities vanish, with a step size of 0.5 bohr. The b_{max} values are 13.5(13.0), 11.5(11.5), 11.0(10.5), and 9.5(9.0) bohr for the $F^- + CH_3I(CD_3I)$ reactions at the above collision energies, respectively. The initial orientation of the reactants is random, and the trajectories are initiated from the vibrational ground states of the polyatomic reactants by setting their zero-point vibrational energies using standard normal-mode sampling[54]. The initial rotational angular momentum of the reactants is set to zero by standard modification of the velocities. Five thousand trajectories were run for each impact parameter-collision energy pair.

The cross sections of the reactions at different collision energies are obtained with a b-weighted numerical integration of the opacity functions. The scattering angle distribution of the products is calculated by binning the cosine of the included angle θ of the relative velocity vector of the reactants and that of the products into 10 equidistant bins, where backward scattering corresponds to $\cos\theta = -1$.

Quantum scattering calculations

The six-dimensional model for the $X + CH_3Y$ system employed in this study has been presented previously[48] (see Fig. S1 in the supplementary information). The 6D model Hamiltonian for the $F^- + CH_3I$ reaction is written as ($\hbar = 1$),

$$\widehat{H} = \frac{-1}{2\mu_R}\frac{\partial^2}{\partial R^2} + \frac{\left(\widehat{J}_{tot} - \widehat{J}\right)^2}{2\mu_R R^2} + \widehat{K}^{vib}_{CH_3I} + \widehat{K}^{rot}_{CH_3I} + V(R, r, \rho, \gamma, \theta, \varphi). \quad (3)$$

Here, R is the distance from the center of mass of CH_3I to F^-, r is the distance from the center of mass of CH_3 to I. The symmetric CH stretching mode and the umbrella mode of the CH_3 group are described by scaled-polar coordinates (ρ, γ), the rotation of CH_3I in the

body-fixed frame is described by the angles (θ, φ), and μ_R is the reduced mass of the $F^- + CH_3I$ system. $\hat{J}_{tot}$ is the total angular momentum operator of the system and $\hat{J}$ is the rotational angular momentum operator of CH_3I. $\hat{K}^{vib}_{CH_3I}$ and $\hat{K}^{rot}_{CH_3I}$ are the vibrational and rotational kinetic energy operators of CH_3I, respectively. The last term $V(R, r, \rho, \gamma, \theta, \varphi)$ is the potential energy[37]. The operators are described in detail in the supplementary information.

The initial wave packet is constructed as the direct product of a localized wave packet $G^0(R)$ and the eigenfunction of CH_3I specified by (n_0, J_0, k_0, K_0, p_0), which represent the initial vibrational quantum number, initial rotational quantum number of CH_3I, the projection of J_0 on the C_{3v} symmetry axis, the projection of J_{tot} on the body-fixed z-axis, and the parity of CH_3I, respectively. $G^0(R)$ is chosen to be a Gaussian function,

$$G^0(R) = \left(\pi\delta^2\right)^{-1/4} \exp\left[\frac{-(R-R_0)^2}{2\delta^2}\right] \exp\left(-i\sqrt{2\mu_R E_0}R\right), \quad (4)$$

where R_0 and δ are the center and width of the Gaussian function, and E_0 is the mean collision energy. The wave packet is propagated using the split operator method[55].

Data availability

The data generated in this study have been deposited in the zenodo database under https://doi.org/10.5281/zenodo.8195586 [https://doi.org/10.5281/zenodo.8195586]. Source data for the figures are provided as a Source Data file. Source data are provided with this paper.

References

1. Bohme, D. K. & Young, L. B. Kinetic studies of reactions of oxide, hydroxide, alkoxide, phenyl, and benzylic anions with methyl chloride in gas phase at 22.5 degrees. *J. Am. Chem. Soc.* **92**, 7354 (1970).
2. Olmstead, W. N. & Brauman, J. I. Gas-phase nucleophilic displacement reactions. *J. Am. Chem. Soc.* **99**, 4219–4228 (1977).
3. Hase, W. L. Simulations of gas-phase chemical reactions: applications to S_N2 nucleophilic substitution. *Science* **266**, 998–1002 (1994).
4. Laerdahl, J. K. & Uggerud, E. Gas phase nucleophilic substitution. *Int. J. Mass Spectrom.* **214**, 277–314 (2002).
5. Xie, J. et al. Identification of atomic-level mechanisms for gas-phase $X^- + CH_3Y$ S_N2 reactions by combined experiments and simulations. *Acc. Chem. Res.* **47**, 2960–2969 (2014).
6. Wester, R. Fifty years of nucleophilic substitution in the gas phase. *Mass Spectrom. Rev.* **41**, 627–644 (2022).
7. Mikosch, J. et al. Imaging nucleophilic substitution dynamics. *Science* **319**, 183–186 (2008).
8. Zhang, J. et al. $F^- + CH_3I \rightarrow FCH_{3+I^-}$ reaction dynamics. nontraditional atomistic mechanisms and formation of a hydrogen-bonded complex. *J. Phys. Chem. Lett.* **1**, 2747–2752 (2010).
9. Mikosch, J. et al. Indirect dynamics in a highly exoergic substitution reaction. *J. Am. Chem. Soc.* **135**, 4250–4259 (2013).
10. Szabó, I. & Czakó, G. Revealing a double-inversion mechanism for the $F^- + CH_3Cl$ S_N2 reaction. *Nat. Commun.* **6**, 5972 (2015).
11. Stei, M. et al. Influence of the leaving group on the dynamics of a gas-phase S_N2 reaction. *Nat. Chem.* **8**, 151–156 (2016).
12. Szabó, I., Olasz, B. & Czakó, G. Deciphering front-side complex formation in S_N2 reactions via dynamics mapping. *J. Phys. Chem. Lett.* **8**, 2917–2923 (2017).
13. Townsend, D. et al. The roaming atom: straying from the reaction path in formaldehyde decomposition. *Science* **306**, 1158–1161 (2004).
14. Heazlewood, B. R. et al. Roaming is the dominant mechanism for molecular products in acetaldehyd e photodissociation. *Proc. Natl. Acad. Sci. USA.* **105**, 12719 (2008).
15. Continetti, R. E. & Guo, H. Dynamics of transient speciesviaanion photodetachment. *Chem. Soc. Rev.* **46**, 7650–7667 (2017).
16. Pan, H., Wang, F., Czakó, G. & Liu, K. Direct mapping of the angle-dependent barrier to reaction for $Cl + CHD_3$ using polarized scattering data. *Nat. Chem.* **9**, 1175–1180 (2017).
17. Foley, C. D., Xie, C., Guo, H. & Suits, A. G. Orbiting resonances in formaldehyde reveal coupling of roaming, radical, and molecular channels. *Science* **374**, 1122 (2021).
18. Meyer, J. et al. Atomistic dynamics of elimination and substitution reactions disentangled. *Nat. Chem.* **13**, 977–981 (2021).
19. Althorpe, S. C. & Clary, D. C. Quantum scattering calculations on chemical reactions. *Annu. Rev. Phys. Chem.* **54**, 493 (2003).
20. Yang, T. et al. Extremely short-lived reaction resonances in Cl + HD(v = 1) → DCl + H due to chemical bond softening. *Science* **347**, 60–63 (2015).
21. Zhang, X., Li, L., Chen, J., Liu, S. & Zhang, D. H. Feshbach resonances in the $F + H_2O \rightarrow HF + OH$ reaction. *Nat. Commun.* **11**, 223 (2020).
22. Yuan, D. et al. Observation of the geometric phase effect in the H + HD → H2 + D reaction below the conical intersection. *Nat. Commun.* **11**, 3640 (2020).
23. Chen, W. et al. Quantum interference between spin-orbit split partial waves in the F + HD → HF + D reaction. *Science* **371**, 936 (2021).
24. Wild, R., Nötzold, M., Simpson, M., Tran, T. D. & Wester, R. Tunneling measured in a very slow ion-molecule reaction. *Nature* **615**, 425 (2023).
25. Hoppe, H. & Manthe, U. First-principles theory for the reaction of chlorine with methane. *J. Phys. Chem. Lett.* **13**, 2563–2566 (2022).
26. Viggiano, A. et al. Temperature dependence of the kinetic isotope effect for a gas-phase S_N2 reaction: Cl^- + CH_3Br. *J. Am. Chem. Soc.* **113**, 9404–9405 (1991).
27. O'Hair, R. A. J. et al. Measurements of solvent and secondary kinetic isotope effects for the gas-phase S_N2 reactions of fluoride with methyl halides. *J. Am. Chem. Soc.* **116**, 3609–3610 (1994).
28. Kato, S., Davico, G. E., Lee, H. S., DePuy, C. H. & Bierbaum, V. M. Deuterium kinetic isotope effects in gas phase S_N2 reactions. *Int. J. Mass Spectrom.* **210/211**, 223–229 (2001).
29. Kato, S., Hacaloglu, J., Davico, G. E., DePuy, C. H. & Bierbaum, V. M. Deuterium kinetic isotope effects in the gas-phase S_N2 reactions of solvated fluoride ions with methyl halides. *J. Phys. Chem.* **108**, 9887 (2004).
30. Zhao, Z., Zhang, Z., Liu, S. & Zhang, D. H. Dynamical barrier and isotope effects in the simplest substitution reaction via Walden inversion mechanism. *Nat. Commun.* **8**, 1–7 (2017).
31. Zhang, B., Shiu, W. & Liu, K. Imaging the reaction dynamics of OH + CD_4. 3. isotope effects. *J. Phys. Chem. A* **109**, 8989–8993 (2005).
32. Espinosa-Garcia, J. & Corchado, J. C. Product translational and vibrational distributions for the OH/OD + CH_4/CD_4 reactions from quasiclassical trajectory calculations. comparison with experiment. *J. Phys. Chem. B* **120**, 1446–1453 (2016).
33. Yan, S., Wu, Y.-T., Zhang, B., Yue, X.-F. & Liu, K. Do vibrational excitations of CHD_3 preferentially promote reactivity toward the chlorine atom? *Science* **316**, 1723–1726 (2007).
34. Wang, F., Lin, J.-S. & Liu, K. Steric control of the reaction of CH stretch-excited CHD_3 with chlorine atom. *Science* **331**, 900–903 (2011).
35. Su, T., Morris, R. A., Viggiano, A. A. & Paulson, J. F. Kinetic energy and temperature dependences for the reactions of fluoride with halogenated methanes: experiment and theory. *J. Phys. Chem.* **94**, 8426–8430 (1990).
36. Zhang, J. & Hase, W. L. Electronic structure theory study of the F^- + $CH_3I \rightarrow CH_3Cl + F^-$ potential energy surface. *J. Phys. Chem. A* **114**, 9635–9643 (2010).
37. Olasz, B., Szabó, I. & Czakó, G. High-level ab initio potential energy surface and dynamics of the F^- + CH_3I S_N2 and proton-transfer reactions. *Chem. Sci.* **8**, 3164–3170 (2017).

38. Stei, M. et al. Stretching vibration is a spectator in nucleophilic substitution. *Sci. Adv.* **4**, 9544 (2018).
39. Michaelsen, T. et al. The influence of vibrational excitation on the reaction of F^- with CH_3I: Spectator mode behavior, enhancement and suppression. *J. Phys. Chem. Lett.* **11**, 4331–4336 (2020).
40. Michaelsen, T., Bastian, B., Strübin, P., Meyer, J. & Wester, R. Proton transfer dynamics modified by CH-stretching excitation. *Phys. Chem. Chem. Phys.* **22**, 12382–12388 (2020).
41. Otto, R. et al. Single solvent molecules can affect the dynamics of substitution reactions. *Nat. Chem.* **4**, 534–538 (2012).
42. Walden, P. Über die gegenseitige Umwandlung optischer Antipoden. *Ber. Dtsch. Chem. Ges.* **29**, 133–138 (1896).
43. Zhang, J., Xie, J. & Hase, W. L. Dynamics of the $F^- + CH_3I \rightarrow HF + CH_2I^-$ proton transfer reaction. *J. Phys. Chem. A* **119**, 12517–12525 (2015).
44. Carrascosa, E. et al. Imaging proton transfer and dihalide formation pathways in reactions of $F^- + CH_3I$. *J. Phys. Chem. A* **120**, 4711–4719 (2016).
45. Gadhi, J., Wlodarczak, G., Legrand, J. & Demaison, J. The dipole moments of methyl bromide and methyl iodide. *Chem. Phys. Lett.* **156**, 401–404 (1989).
46. Cheon, S., Song, K. & Hase, W. L. Central barrier recrossing dynamics of the $Cl^- + CD_3Cl$ S_N2 reaction. *J. Mol. Struct.* **771**, 27 (2006).
47. Manikandan, P., Zhang, J. & Hase, W. L. Chemical dynamics simulations of $X^- + CH_3Y \rightarrow XCH_3 + Y^-$ gas-phase S_N2 nucleophilic substitution reactions. nonstatistical dynamics and nontraditional reaction mechanisms. *J. Phys. Chem. A* **116**, 3061–3080 (2012).
48. Wang, Y. et al. Mode-specific S_N2 reaction dynamics. *J. Phys. Chem. Lett.* **7**, 3322–3327 (2016).
49. Olasz, B. & Czakó, G. Mode-specific quasiclassical dynamics of the $F^- + CH_3I$ S_N2 and proton-transfer reactions. *J. Phys. Chem. A* **122**, 8143–8151 (2018).
50. Collepardo-Guevara, R., Suleimanov, Y. V. & Manolopoulos, D. E. Bimolecular reaction rates from ring polymer molecular dynamics. *J. Chem. Phys.* **130**, 174713 (2009).
51. Wester, R. Velocity map imaging of ion–molecule reactions. *Phys. Chem. Chem. Phys.* **16**, 396–405 (2014).
52. Meyer, J. & Wester, R. Ion-molecule reaction dynamics. *Annu. Rev. Phys. Chem.* **68**, 333–353 (2017).
53. Carrascosa, E., Meyer, J. & Wester, R. Imaging the dynamics of ion–molecule reactions. *Chem. Soc. Rev.* **46**, 7498–7516 (2017).
54. Hase, W. L. Classical trajectory simulations: Final conditions and Classical trajectory simulations: Initial conditions, In *Encyclopedia of Computational Chemistry*, Vol. 1 (ed. Allinger, N.L.) 399–407. (Wiley, New York, 1998).
55. Feit, M. D. & Fleck, Jr,J. A. Solution of the Schrödinger equation by a spectral method II: vibrational energy levels of triatomic molecules. *J. Chem. Phys.* **78**, 301–308 (1983).

Acknowledgements

This work has been supported by the Austrian Science Fund (FWF) through the Doctoral Programme Atoms, Light, and Molecules, Project No. W1259-N27, and by the European Research Council (ERC) under the European Union's Horizon 2020 research and innovation programme (grant agreement No. 885479). D.P. and G.C. thank the National Research, Development and Innovation Office-NKFIH, K-125317 and K-146759; Project No. TKP2021-NVA-19, provided by the Ministry of Culture and Innovation of Hungary from the National Research, Development and Innovation Fund, financed under the TKP2021-NVA funding scheme; and the Momentum (Lendület) Program of the Hungarian Academy of Sciences for the financial support. D. P. thanks the National Research, Development and Innovation Office - NKFIH, STARTING 150749. This work was also supported by the National Natural Science Foundation of China (Grant Nos. 21963008 to Y.W., 21973109 to H.S., and 21973108, 22373111, and 21921004 to M.Y.).

Author contributions

A.A., A.K., T.G., and T.M. performed the experiment, A.A., A.K., and T.M. analyzed the data, R.W. supervised the project, D.P. and G.C. carried out the QCT simulations, Y.W., H.S., and M.Y. performed the quantum dynamics calculations, A.A. and R.W. wrote the manuscript.

Competing interests

The authors declare no competing interest.

Additional information

Supplementary information The online version contains supplementary material available at https://doi.org/10.1038/s41467-025-57086-0.

Correspondence and requests for materials should be addressed to Roland Wester.

Peer review information *Nature Communications* thanks the anonymous reviewer(s) for their contribution to the peer review of this work. A peer review file is available.